Alma Mater Studiorum · Università di Bologna

Scuola di Scienze
Dipartimento di Fisica e Astronomia
Laurea in Fisica

Faulting processes in a poro–elastic half–space

RELATORE
Prof. Maria Elina Belardinelli

CO–RELATORE
Dott. Massimo Nespoli

AUTORE
Giovanni Gravili

Anno Accademico 2022/2023

Sommario

L'obiettivo di questa tesi è di simulare i processi di fagliazione in un semispazio poro–elastico tramite un approccio numerico, l'implementazione del quale è presente nei programmi *pegrn*/*pecmp*. In questa tesi sono stati studiati i tipi di faglia trascorrente, normale e inversa. I campi di spostamento superficiale co–sismico e post–sismico e di pressione di poro in profondità sono stati calcolati e visualizzati in sezioni orizzontali. Nel primo capitolo è stata introdotta la teoria elastica, presentando le relazioni costitutive elastiche per lo sforzo e la deformazione. Successivamente, è stata presentata la teoria della poro–elasticità che ci permette di tener conto della presenza di fluidi nei pori delle rocce. Nella sezione successiva, vengono introdotti i meccanismi di fagliazione e gli ambienti tettonici. Questo ci permette di determinare le geometrie di faglia che possono essere attese in base all'ambiente tettonico. Tramite l'assunzione di un semispazio omogeneo poro–elastico, i tre differenti tipi di faglie sono stati studiati. Prima di riportare i risultati, viene specificata configurazione dei programmi.

Abstract

The focus of this thesis is to simulate the faulting processes in a poro–elastic half–space through numerical approach, the implementation of which is present in the programs *pegrn/pecmp*. In this thesis the strike–slip, normal and thrust fault types are studied. The surface co–seismic and post–seismic displacement and pore–pressure fields at depth are computed and plotted in horizontal section maps. In the first chapter the elastic theory has been discussed, introducing the elastic constitutive relations for stress and strain. Next, the theory of poro–elasticy has been introduced which allows us to study the presence of fluids in the pores of the rocks. In the next section, the faulting mechanisms and the tectonic environments are introduced. This allows us to determine the fault geometries that can be expected depending on the tectonic environment. Through the assumption of a homogeneous poro–elastic half–space, the three different fault types have been studied. Before reporting the results, the configuration of the programs is given.

Contents

Chapter 1

Introduction

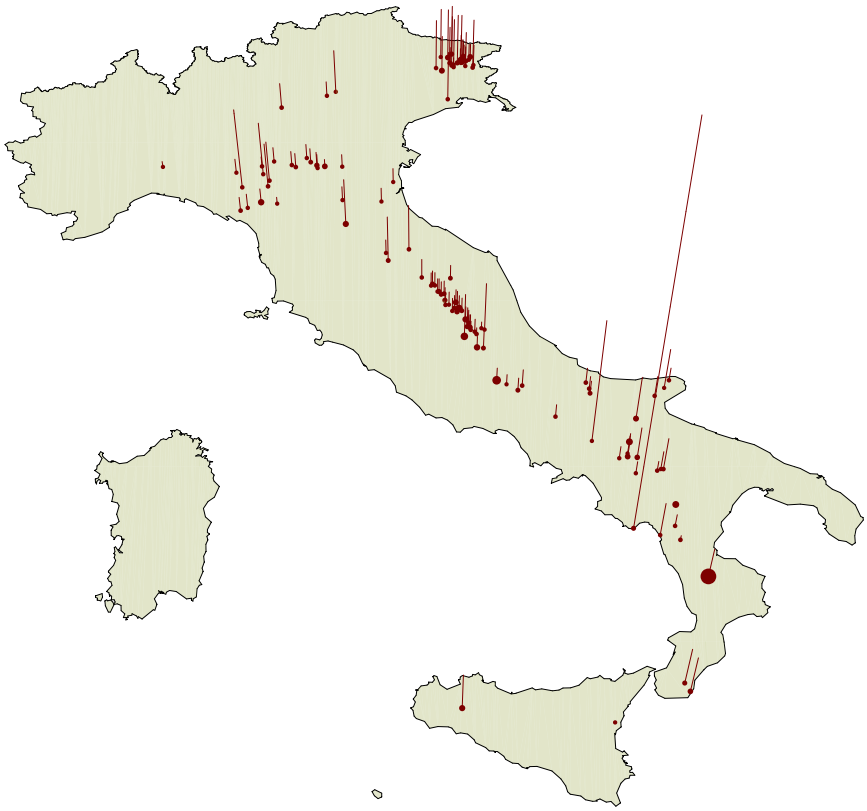

Figure 1.1: Distribution of the earthquake hypocenters with Richter magnitude 5 and higher that took place in Italy in the last century. The image intends to give an idea of the scale of the phenomena: the vertical lines represent the quake's depth, while the point size illustrates the magnitude relative to Richter magnitude 9 quakes and the location of epicenter of the event, an adaptation from Wolfram (2023).

The purpose of this thesis is the characterisation of the poro–elastic rebound due to strike–slip, normal and thrust fault types in a poro–elastic half–space. Poro–elastic rebound is a process which can be observed at the surface in terms of a displacement

field varying as a function of time, in *near field* conditions, that is at a distance from the epicenter (*e.g.* Fig. 1) smaller than the source fault dimension. Faults are surface discontinuities of the crust which host the nucleation point, also called hypocenter, of an earthquake process. For this reason faults are also called earthquake sources. With the aid of software made by Wang and Kümpel (2003) implementing the equations of poro–elasticity, the rebound phenomena is accurately simulated and the results presented.

In order to properly model the phenomena, following the theory of poro–elasticity by Biot (1941), it is necessary to account for the presence of fluids in the medium. Specifically, if it is mainly composed by rocks, then the fluids have to reside in embedded sacks known as pore, which inevitably become interconnected over time due to the natural tendency of the fluid to erode and infiltrate. In this chapter the strain and stress tensors and the constituive equation relating them in the case of elastic and poro–elastic media are introduced. Finally we introduce fault features related to the principal tectonic environments.

1.1 Strain and stress tensors

The small deformations of a body are expressed by the elastic strain tensor, given by the symmetric part of the displacement gradient,

$$\varepsilon_{ij} = \frac{1}{2}\left(\frac{\partial u_i}{\partial x_j} + \frac{\partial u_j}{\partial x_i}\right) \text{ if } \left|\frac{\partial u_i}{\partial x_j}\right| \ll 1. \tag{1.1}$$

Its diagonal components give the relative variation in length along x_1, x_2 and x_3 axes.

Due to its symmetry, the eigenvalue λ borne out of the related eigensystem

$$\varepsilon_{ij} n_j = \lambda n_i \tag{1.2}$$

equally measures the relative variation in length along the so–called principal axis $\hat{\mathbf{n}}$.

1.1.1 Decomposition of the strain tensor

Each tensor can be split into so–called deviatoric and isotropic components. The deviatoric part is constructed as trace–less, while the trace is used to construct a diagonal tensor.

The elastic strain tensor ε_{ij} is then separated into a superposition of a deviatoric part, altering solely the shape of the body, and an isotropic deformation associated to the volume change, the isotropic part, as given in Greenshields and Weller (2022),

$$\varepsilon_{ij} = \left(\varepsilon_{ij} - \frac{\varepsilon_{kk}}{3}\delta_{ij}\right) + \frac{\varepsilon_{kk}}{3}\delta_{ij}. \tag{1.3}$$

The trace of the strain tensor ε_{kk} gives the relative variation in volume due to a deformation. Thus, when the trace is zero, only the shape of the body is being altered and the forces causing it are said of pure shear.

The first component in the strain tensor decomposition as in Eq. (1.3) is identified as its deviatoric component, giving the variation in shape of the body, while its second component only characterises the relative variation in volume.

1.1.2 Stress tensor

The surface force field T_i acting on a surface with normal $\hat{\mathbf{n}}$ per unit area, measured in $[T_i]$ =Pa and identified as the traction, is obtained by projecting the local normals n_i to the body onto a field τ_{ij},

$$T_i = \tau_{ij} n_j. \tag{1.4}$$

This field τ_{ij} is known as the stress tensor, and its unit of measurement is obtained from the previous relationship, $[\tau_{ij}] = \text{Pa}$, as the normals are taken unit–less.

The stress tensor is symmetric and thus, diagonalisable by means of the eigensystem

$$\tau_{ij} n_j = \sigma n_i, \tag{1.5}$$

where $\hat{\mathbf{n}}$ are the eigenvectors, giving the so–called principal axes.
The three eigenvalues σ are identified as the principal values.

The stress tensor is also decomposable in a deviatoric and isotropic part,

$$\tau_{ij} = \left(\tau_{ij} - \frac{\tau_{kk}}{3}\delta_{ij}\right) + \frac{\tau_{kk}}{3}\delta_{ij}. \tag{1.6}$$

The isotropic component gives the average normal force per unit of area, identified as minus the mean pressure, while its deviatoric component encodes the tangential forces responsible for the shape variations, known as the shear forces.

1.1.3 Work of deformation

The strain and stress tensors are linearly dependent in the regime of small–deformations. On the contrary, the experimentally measured stress–strain relationship isn't linear after a certain ratio threshold has been met. This fact explains how plastic and elastic deformations can both coexist. The first ones are characterised by being spontaneously irreversible, and thus have a non–zero deformation work W spent to perform a cyclic transformation.

Working with the assumption of elastic behaviour requires all deformation processes to be adiabatic or isothermic transformations. In our case, temperature does not vary and neither does the total work of deformation, as shown in the work of Landau et al. (1986),

$$W = \oint \tau_{ij}\, \mathrm{d}\varepsilon_{ij} = 0, \text{ where } \mathrm{d}W = \tau_{ij}\, \mathrm{d}\varepsilon_{ij}. \tag{1.7}$$

This means that it is not possible to permanently store any energy in an elastic material, as it will spontaneously revert to its initial configuration of no deformation.

In practice, elastic deformation processes are isotherms under the assumption that the rate of deformation is much lower than the rate of propagation of the thermal equilibrium. Under this assumption, the body continuously deforms at a constant temperature.

1.1.4 Stress–strain elastic constitutive equations

The stress tensor is linearly dependent on the strain tensor in the limit of elastic behaviour. For an elastic isotropic body, the moduli of compression K and rigidity μ are the sole needed to determine the strain–stress relations,

$$\tau_{ij} = K\varepsilon_{kk}\delta_{ij} + 2\mu\left(\varepsilon_{ij} - \frac{\varepsilon_{kk}}{3}\delta_{ij}\right). \tag{1.8}$$

The elastic parameter K, the bulk modulus or modulus of hydrostatic compression, is calculated as

$$K = \lambda + \frac{2}{3}\mu, \tag{1.9}$$

and is measured in $[K] = \text{Pa}$.

The coefficients λ and μ on which it depends here introduced are identified as the Lamé elastic parameters. Their units of measurement are $[\lambda] = [\mu] = \text{Pa}$ and a typical range of values is of the order of GPa for the rocks of the crust.

The velocity of the primary and secondary waves v_1, v_2 in earthquakes are functions of the Lamè elastic parameters,

$$v_1 = \sqrt{\frac{\lambda + 2\mu}{\rho}}, \quad v_2 = \sqrt{\frac{\mu}{\rho}}, \tag{1.10}$$

where ρ is the density of the medium in which the waves propagate.

Role of the elastic parameters

The bulk modulus K determines the relative variation in volume of the body in the ways prescribed by the equation

$$\varepsilon_{kk} = \frac{\tau_{kk}}{3K}, \tag{1.11}$$

derived from the stress–strain relationship Eq. (1.8), as the trace of the second term is zero.

One can find that due to the linearity of the strain–stress relations, the inverse constitutive equation is given by

$$\varepsilon_{ij} = \frac{\tau_{kk}}{9K}\delta_{ij} + \frac{1}{2\mu}\left(\tau_{ij} - \frac{\tau_{kk}}{3}\delta_{ij}\right). \tag{1.12}$$

1.1.5 Young's modulus and Poisson's ratio

Isotropic elastic media can be characterised by different couples of parameters.

For instance, for the case of a vertical displacement of a rod under the traction τ_{33} applied along its axis of symmetry, x_3, the relative variation in length of the rod is given by the component of the strain tensor,

$$\varepsilon_{33} = \frac{\tau_{33}}{E}. \tag{1.13}$$

The parameter E introduced is Young's modulus of extension or compression. Such coefficient gives us means of estimating how much an increase in the applied traction results in a deformation. It is given by the expression

$$E = \frac{9K\mu}{3K + \mu}, \tag{1.14}$$

measured in the same units as pressure, $[E] = \text{Pa}$.

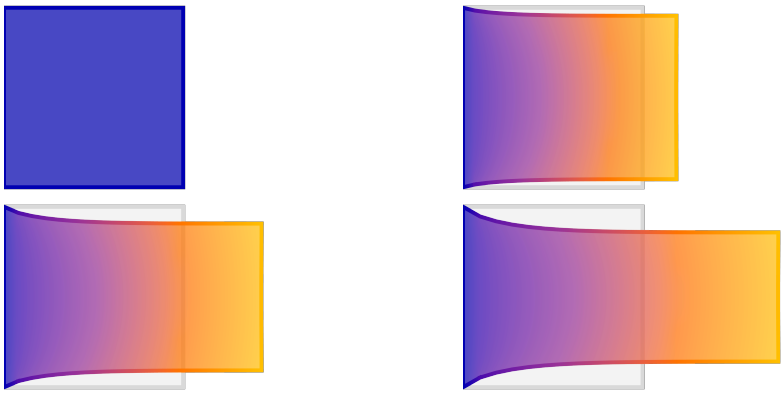

Figure 1.2: Various stages of the elastic deformation for an ideal elastic material. The block is fixed on the left by a support while being subjected to a tensile load of various force magnitudes in its rightmost extremity, by Wolfram (2022).

In this case of homogeneous vertical deformation, with x_3 as axis of symmetry, it is found that along the transverse directions the other diagonal components of the strain tensor have to be equal in magnitude. By using Eq. (1.12), such components are found to be linked to the relative variation in length through the formula

$$\varepsilon_{11} = \varepsilon_{22} = -\nu\varepsilon_{33}, \tag{1.15}$$

where the ratio of the transverse compression to the longitudinal extension is defined as Poisson's ratio ν. It takes values in the range between -1 and 1/2,

$$\nu = \frac{3K - 2\mu}{6K + 2\mu}, \tag{1.16}$$

and it does not have a unit of measurement.

Thanks to Eq. (1.16), the Eq. (1.12) can be expressed as

$$\varepsilon_{ij} = \frac{1}{2\mu}\left(\tau_{ij} - \frac{\nu}{1+\nu}\tau_{kk}\delta_{ij}\right). \tag{1.17}$$

1.2 Theory of poro–elasticity

Sponges are optimal examples of poro–elastic media, and this is because their porous structure, within which fluids can infiltrate and reside in, is able to spontaneously regain its shape after being deformed.

In order to describe such a structure, fluid–mechanical theories have to be included into the theory of elasticity. This is done by means of including an additional fluid–related element in the work of deformation Belardinelli and Bonafede (2022),

$$\mathrm{d}W = \tau_{ij}\,\mathrm{d}\varepsilon_{ij} + p\,\mathrm{d}v, \tag{1.18}$$

where p is the pressure of the fluid inside the pores, known as the pore–pressure in the theory of poro–elasticity, and v is the volume of fluid per unit of volume of medium, and thus does not have an associated unit of measurement.

1.2.1 Constitutive equations

To derive the strain–strain relations for a poro–elastic medium, the linearity is exploited to represent the general deformation as a superposition of effects.

If the pore–pressure is zero, the equations are the ones of elasticity given by Eq. (1.17), where the coefficients are the modulus of rigidity μ and Poisson's ratio ν.

In order to keep the pore–pressure constantly zero, as assumed, the volume of fluid v has to vary if a stress is applied. Specifically, it varies proportionately to the applied stresses,

$$v = \frac{\tau_{kk}}{3H}. \tag{1.19}$$

The constant of proportionality H here introduced is such that its inverse gives exactly the volume of fluid expelled by an unitary volume of material after the application of a an unitary confinement pressure p_C, given by

$$p_C = -\frac{\tau_{kk}}{3}. \tag{1.20}$$

On the other hand, by enforcing a constant and uniform stress field τ_{ij}, the strain tensor has to vary proportionately to the pore–pressure,

$$\varepsilon_{ij} = \frac{p}{3H}\delta_{ij}. \tag{1.21}$$

The proportionality coefficient H is exactly the one previously introduced, although in this context it gives the relative increment in volume of an unitary volume element of the medium due to an unitary increment in the pore–pressure, while the stress field is kept null. It is then measured in $[H]$ =Pa, as is the pore–pressure.

The relative variation of the fluid volume is linearly dependent on the pore–pressure under such assumptions,

$$v = \frac{p}{R}. \tag{1.22}$$

The parameter R gives the relative variation of fluid volume inside the medium due to an expansion or contraction of the pores set off by an unitary increase of the pore–pressure. It is measured in $[R]$ =Pa, as v is unit–less.

Consequently, by the assumed linearity of the strain–stress relations, the separately studied effects can be superimposed to yield the general–case deformation scenario, given by the simultaneous equations

$$\varepsilon_{ij} = \frac{1}{2\mu}\left(\tau_{ij} - \frac{\nu}{1+\nu}\tau_{kk}\delta_{ij}\right) + \frac{p}{3H}\delta_{ij}, \tag{1.23}$$

$$v = \frac{\tau_{kk}}{3H} + \frac{p}{R}. \tag{1.24}$$

1.3 Poro–elastic coefficients

It is found that to these equations are associated the extensions of Young's modulus E and Poisson's ratio ν to poro–elasticity, identified as the drained coefficients.

Undrained regime takes place when the medium has no outflow of fluid and thus, the system loses no mass, Wang and Manga (2021).

By increasing the pore–pressure, the material expands as the fluid pushes against the inner surfaces of the pores. On the contrary, by increasing the confinement pressure p_C, the material contracts. This is expressed by means of the strain tensor's trace,

$$\varepsilon_{kk} = \frac{1-2\nu}{2\mu(1+\nu)}\tau_{kk} + \frac{p}{H}, \tag{1.25}$$

where the drained incompressibility K is,

$$K = -V\frac{\partial p_c}{\partial V}\Big|_{p=0} = \frac{\tau_{kk}}{3\varepsilon_{kk}}\Big|_{p=0} = \frac{2\mu(1+\nu)}{3(1-2\nu)}, \tag{1.26}$$

and is measured in $[K] = \text{Pa}$.

Furthermore, the expression for Young's drained modulus E is found by subjecting the body to uniaxial traction,

$$E = \frac{\tau_{11}}{\varepsilon_{11}}\Big|_{p=0} = 2\mu(1+\nu). \tag{1.27}$$

For an elastic and pore–less material under the effect of an external balancing pressure field equal to the internal pore–pressure $\tau_{ij} = -p\delta_{ij}$, the strain tensor at equilibrium is given by

$$\varepsilon_{ij} = -\frac{p}{3K_S}\delta_{ij}. \tag{1.28}$$

The coefficient K_S is the incompressibility for the solid matrix.

Through direct substitution into the constitutive equations Eq. (1.23) and (1.24), a correlation between the elastic and poro–elastic parameters emerges,

$$\frac{1}{H} = \frac{1}{K} - \frac{1}{K_S}. \tag{1.29}$$

While, from an analysis of the pores' volume variation, the following is established

$$\frac{1}{R} = \frac{1}{H} - \frac{1}{K_S}, \tag{1.30}$$

where v_0 is the initial volume of fluid present in the pores.

1.3.1 Skempton's coefficient

In the regime of compressible flow, the fluid's relative density varies proportionally to the pressure it undergoes,

$$\frac{\Delta\rho}{\rho} = \frac{p}{K_F}, \tag{1.31}$$

where K_F is the coefficient of incompressibility for the fluid.

Through this result, the variation in fluid mass is evaluated by its associated differential equation. Assuming that no fluid mass is lost from the application of an impulsive stress field τ_{ij}, working in the undrained regime, an associated pore–pressure p is generated,

$$p = -\frac{B}{3}\tau_{kk}, \tag{1.32}$$

where B is known as Skempton's coefficient.

It is given by the inverses of the previously introduced elastic coefficients,

$$B = \frac{KK_F}{K_F\left(K - Hv_0\right) + HKv_0}. \tag{1.33}$$

To better understand its significance, in a very porous matrix where the fluid is still in its liquid phase, such as in sedimentary materials next to the surface, Skempton's coefficient is approximately unitary.

The coefficient takes the value of

$$B \approx \frac{R}{H} \tag{1.34}$$

when the solid or fluid phases of the fluid are extremely compressible.

Skempton's coefficient models the undrained Poisson's ratio ν_u, as $B = 1$ gives the maximum value of ν_u and $B = 0$ gives the lowest.

In undrained conditions, Rice and Cleary (1976) gives the poro–elastic equations

$$\varepsilon_{ij} = \frac{1}{2\mu}\left(\tau_{ij} - \frac{\nu}{1+\nu}\tau_{kk}\delta_{ij} + \frac{3(\nu_u - \nu)}{B(1+\nu)(1+\nu_u)}p\delta_{ij}\right) \tag{1.35}$$

In the early stages after a earthquake's (postseismic stages), a transition of the soil from an undrained to a drained regime takes place as the fluid begins to flow due to the acting stresses. This means that the poro–elastic equations have to be solved in the post–seismic phase.

1.3.2 Darcy's law and hydraulic diffusivity

The motion of fluids in porous and permeable media is described by Darcy's law.

In a configuration in which a reservoir of fluid is suspended at a certain height and forced to flow downwards through a porous and permeable material, if a pressure gradient due to gravity is present, then the flux of the fluid is proportional to the effective pressure gradient $\nabla p^* = \nabla p - \rho_f g$. Particularly, if the density of the fluid ρ_f is constant, then the effective pressure is given by $p^* = p - \rho_f g z$.

The volume of fluid that goes through the porous and permeable material per unit of area and time q is inversely proportional to the height h of the material column and directly proportional to the difference in effective pressures through the ratio of permeability k and viscosity η,

$$\mathbf{q} = -\frac{k}{\eta}\nabla p^*. \tag{1.36}$$

The vectorial form is a generalisation due to the gradient.

Darcy's law together with the diffusion and equilibrium equations end up defining the quasi–static evolution equation of a poro–elastic material with compressible components,

$$\frac{\partial \tau_{ij}}{\partial x_j} = 0, \quad D\nabla^2\left(\sigma_{kk} + \frac{3p}{B}\right) = \frac{\partial}{\partial t}\left(\sigma_{kk} + \frac{3p}{B}\right), \tag{1.37}$$

where D is the hydraulic diffusivity coefficient, measured in $[D] = \mathrm{m}^2\,\mathrm{s}^{-1}$. The hydraulic diffusity is related to the permeability of the medium.

1.4 Faulting processes

Materials rupture whenever a certain stress threshold is met. This principle is extendable to the study of faulting processes in the crust, as the friction between adjacent blocks of the tectonic plaques, along the fault surfaces, allows for the sudden release of energy, which in turn alters the equilibrium of the fluids residing in the ground.

Faulting events in elastic media are due to a stress configuration with non–vanishing deviatoric part. The rupture happens on a plane intermediate with respect to the ones associated to the eigenvectors relative to the maximum and minimum eigenvalue of the stress tensor.

The first classification of faults is done through the brittle-elastic model which poses a finite resistance to fractures, where the maximum shear stress reaches the threshold value called shear strength of rocks. Once this value is reached, the faulting process takes place and the adjacent blocks undergo a relative sliding along the faulting plane.

Tensile fractures instead take place when the maximum principal stress $\sigma^{(3)}$ is positive and greater than a material–specific threshold. Tensile fractures are characterised by a rupture along the plane of the body, perpendicular to the associated eigenvector for $\sigma^{(3)}$.

The surface of the Earth is assumed stress–free, neglecting the atmospheric pressure and wind shear stresses, and this causes the vertical axis to have an eigenvalue of zero.

At large depth, below the lithosphere, the stress tensor is only given by its isotropic component,

$$\tau_{ij} = -p_{\mathrm{lit}}\delta_{ij} \tag{1.38}$$

where p_{lit} is the lithostatic pressure.

The lithostatic pressure is given as a function of the depth of measurement z, the density of the ground ρ and atmospheric pressure p_{atm},

$$p_{\mathrm{lit}} = \rho g z + p_{\mathrm{atm}}. \tag{1.39}$$

Near the surface, in the lithosphere, the tectonic motions give rise to an additional component h_{ij},

$$\tau_{ij} = h_{ij} - p_{\text{lit}}\delta_{ij}, \tag{1.40}$$

with principal values $\sigma^{(i)}$, given $i = 1, 2, 3$.

The deviatoric component of h_{ij} matches the one of τ_{ij} and is responsible for the ruptures of the rocks, which take place when a certain shear stress threshold is reached, we define

$$\overline{p} = -\frac{\tau_{kk}}{3} = -\frac{h_{kk}}{3} + p_{\text{lit}} \approx p_{\text{lit}}, \quad z \gg 1\,\text{km}. \tag{1.41}$$

The deviatoric stress tensor becomes then $\tau_{ij} + \overline{p}\delta_{ij}$ and its three eigenvalues are $\sigma^{(i)} + \overline{p}$, given $i = 1, 2, 3$. Because it has zero trace, if the eigenvalues are taken to be ordered based on their respective index, then $\sigma^{(1)} + \overline{p}$ is associated to the maximum compression and $\sigma^{(3)} + \overline{p}$ to the maximum tension.

Only in the case of near-surface conditions, due to a limited lithostatic pressure, tensile fractures can happen. Therefore, at larger depths any sort of relative motion of rock blocks during the fracture process must be tangent to the surface of contact of the blocks as it is for a shear fracture.

In the end, it is expected that such fractures happen on planes next to the maximum shear surfaces, although friction can create significant deviations from such directions.

1.5 Faulting mechanisms and tectonic environments

The previous case studies can be applied to the study of faulting environments throughout the lithosphere.

When the resistance of the material is reached, its strength level, a fracture appears on a faulting surface, causing a relative sliding of the two blocks adjacent to the surface itself. These blocks are called as hanging wall and foot wall. In Fig. (1.3) the foot wall is represented.

The geometry of the fault is defined by three angles that constitute its orientation with respect to the axes, oriented to the local geographical directions. The relative displacement of the hanging wall with respect to the foot wall is by us referred to as slip.

Firstly, the strike angle θ of fault plane clockwise from North, can take values in the range $0° \leq \theta \leq 360°$. Then, the dip angle δ of the fault plane down from the horizontal is limited to the values $0° \leq \delta \leq 90°$. Lastly, the rake angle λ in the fault plane is the angle between the slip direction and the strike, in the range $-180° \leq \lambda \leq 180°$.

Additionally, the slip amount along the strike u_θ and dip u_δ direction have to be defined, they give how much the fault slides along the relative direction.

1.5.1 Thrust, normal and strike–slip faults

One has to consider that due to the condition of free–surface, one of the eigenvalues is related to the vertical direction. Depending on which one is in such configuration, different faulting environments are identifiable.

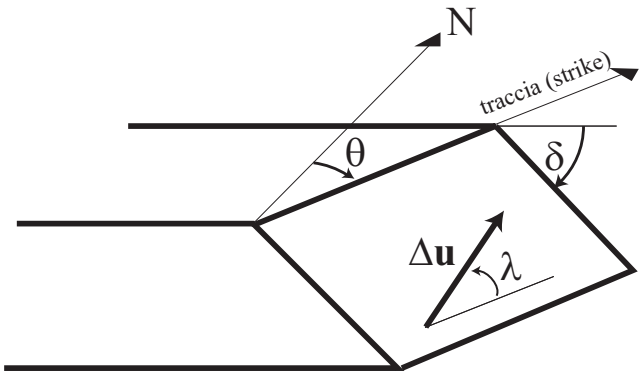

Figure 1.3: Depiction of the fault geometrical configuration dependent on the strike angle θ, the dip angle δ and the rake λ. The slip is given by the vector $\Delta\mathbf{u}$. The fault has length L measured along the strike direction, while its width W is the dimension along the maximum slope direction on the fault surface. The fault surface has length L measured along the strike direction, while its width W is the dimension along the maximum slope direction on the fault surface.

If the vertical axis is related to $\sigma^{(1)} + \overline{p}$, then the axis of maximum tension is horizontal, which lends to a distensive fault environment. The surfaces of maximum shear are tilted by half a right angle with respect to the horizontal direction, which is enough reason for these environments to typically be identified with normal faults, presenting dips greater than 45° due to friction. In this situation the hanging wall slips downwards and the foot wall tends to go up.

In the case of the vertical axis related to $\sigma^{(3)} + \overline{p}$, the axis of maximum compression is horizontal, which gives rise to a compressive environment. The behaviour is opposite to the normal environments, having the foot wall sliding downwards below the hanging wall (thrust fault) going upwards with dip angles smaller than 45°.

Both the axes of maximum tension and compression are horizontal if the vertical axis is the intermediate one associated to $\sigma^{(2)} + \overline{p}$. This gives rise to an horizontal fracture with two perpendicular faults oriented at 45° with respect to the principal stress axes of $\sigma^{(1)}$ and $\sigma^{(3)}$. This causes the maximum shear surfaces to be vertical, therefore, typical of these environments are strike–slip faults, classified in right-handed, or left-handed, depending on the sliding direction of one block with respect to the other.

Taking into account friction, as a shear stress threshold value to reach in order to realise slip on fault surfaces, the dip angle δ is different in the the fault types. This difference emerges more clearly when considering it as a function of the static friction coefficient f_s. The relationship is given by

$$\tan 2\delta = \pm \frac{1}{f_s}, \tag{1.42}$$

which has solutions for both the distensive $(-)$ and compressive environments $(+)$, being $0 < 2\delta < \pi$. Specifically, for $f_s \approx 1$, Anderson's theory predicts $\delta \approx 70°$ for the

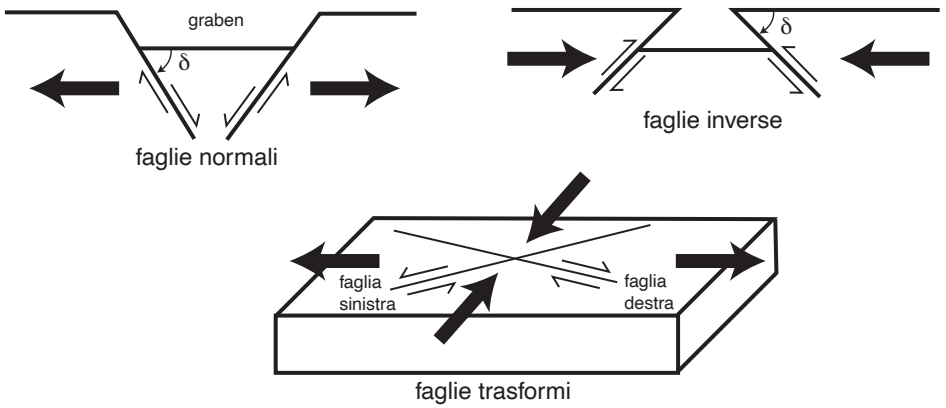

Figure 1.4: Illustration of the strike–slip, normal and thrust fault types highlighting the difference in the dip angle δ between the normal and thrust faults.

normal faults, while for the thrust faults $\delta \approx 20°$.

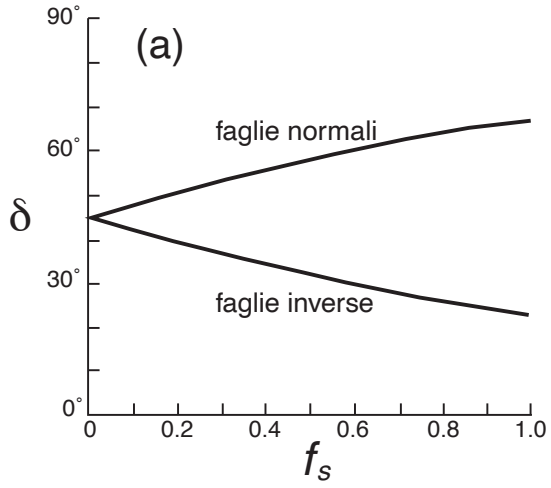

Figure 1.5: Dip angle δ plotted against the static friction coefficient f_s, as predicted by Anderson's theory for normal and thrust faults.

Roccia	G (GPa)	ν	K (GPa)	K_s (GPa)	ϕ	H (GPa)	R (GPa)
Arenaria (Berea)	6.0	0.20	8.0	36.0	19%	10.29	10.88
Arenaria (Weber)	12.2	0.15	13.4	36.0	6%	21.35	22.13
Arenaria (Ruhr)	13.3	0.12	13.1	36.0	2%	20.59	20.83
Granito (Westerly)	15.0	0.25	25.0	45.4	1%	55.64	56.83
Basalto oceanico	30.0	0.25	50.0	83.3	2%	125.1	128.95

Roccia	B	ν	ν_u
Arenaria (Berea)	0.53	0.20	0.31
Arenaria (Weber)	0.64	0.15	0.27
Arenaria (Ruhr)	0.84	0.12	0.30
Granito (Westerly)	0.80	0.25	0.33
Basalto oceanico	0.46	0.25	0.29

Figure 1.6: Table of the poro–elastic parameters for different kinds of rocks, from Wang (2000).

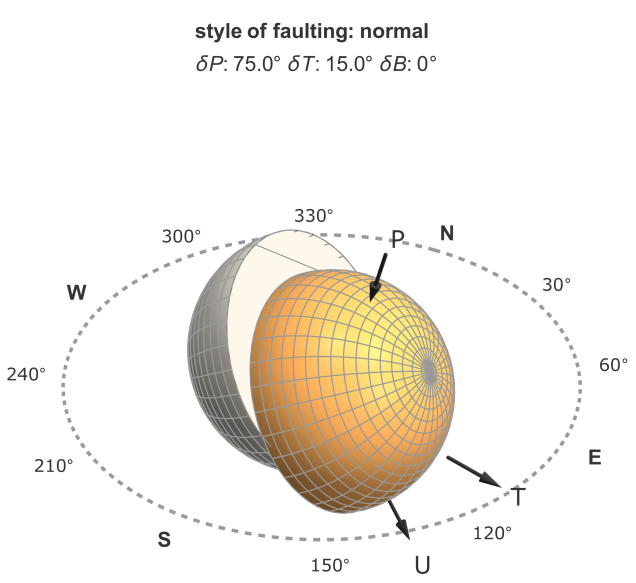

(a) Normal fault, configured to have the geometrical parameters $\theta = 0°, \delta = 60°, \lambda = 90°$.

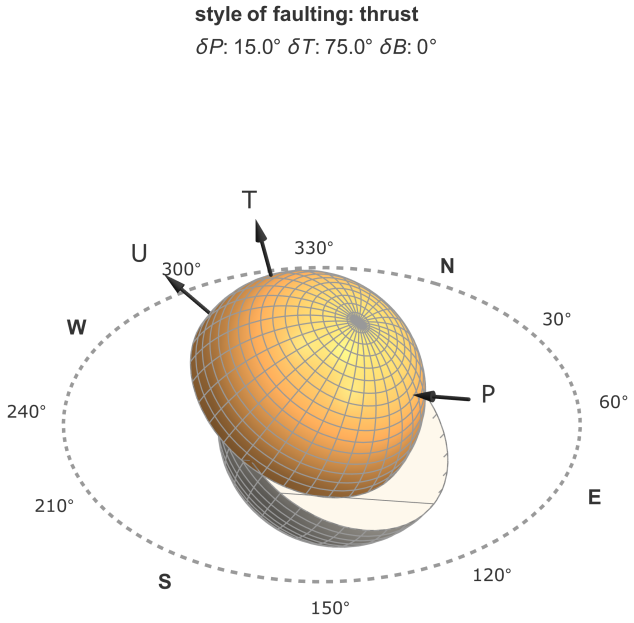

(b) Thrust fault, configured with the geometrical parameters $\theta = 0°, \delta = 30°, \lambda = -90°$.

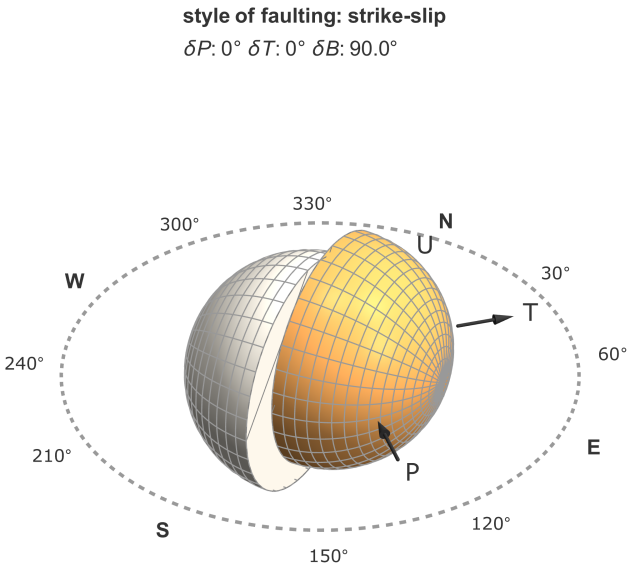

(c) Strike–slip fault, configured to have the geometrical parameters $\theta = 0°, \delta = 90°, \lambda = 0°$.

Figure 1.7: Visualisation of the different types of faults. The plots display the hanging wall and the foot wall against one another. The P and T vectors give the local pressure and tension axes during the faulting process, while U gives the direction in which the hanging wall slips towards. From the works of Scherbaum et al. (2011).

Chapter 2

Presentation of the results

Programs that solve the poro–elastic equations have been developed. Some of them are able to simulate the effects of strike–slip, normal, thrust faults and various others, including any combination thereof , located within poro–elastic media (half–space), which slip at $t = 0$ during an earthquake.

Specifically, the ones by us employed for the simulation of faulting processes are pegrn and pecmp, made by Wang and Kümpel (2003). They employ discretisation techniques which involve the generation of a grid of point–like elements upon which the associated differential equations for poro–elastic media are to be solved and then interpolated.

Interpolation is a process which has the aim of finding the continuous form of a discrete function. It requires the knowledge of a function at certain points, and although originally this function may have a discrete domain, it is then extended to the continuum. The function that the data is interpolated against is an arbitrary choice.

2.1 Process of data retrieval and analysis

Technically, these programs are able to replicate the realistic conditions of faulting environments when given the proper required information, which mainly comprehends the fault's geometry and the poro–elastic parameters, with other various lesser options.

Running the simulations allows us in the end to be able to retrieve the files that contain the simulation data as a time series. This data is then processed in Matlab to produce the contour and vector plots subsequently displayed.

From these files, the pore–pressure p together with Darcy's planar velocities vectors, and the vertical displacement field u_3 together with the planar displacements vectors are retrieved. Such pairings are then used to paint an image of the deformation and the fluid flow in our poro–elastic medium undergoing fracture.

2.2 Configuration of pegrn and pecmp

In order for the simulations to yield consistent results in the different cases, various parameters are shared between the program instances, such as the fault's location and its composition.

Here's the geometrical configuration for the fault:

- The mesh for the generation of the Green's functions is composed of equally spaced elements arranged in a 50×50 grid of physical size given by 200 km length and 100 km depth, with the points separated by 1 km intervals.
- For the plotting to be carried out, the axes have to be changed to the ones of a Cartesian planar representation from the latitude–longitude representation. Technically, this has been achieved in Matlab by employing a function called deg2utm, from the works of Palacios (2023). In this configuration, the fault length is $L = 20\,\mathrm{km}$ and its width is $W = 15\,\mathrm{km}$. The upper border of the faults is located at a depth of 1 km.
- The observations have been carried out at the surface, of depth $z = 0\,\mathrm{km}$ and at a depth of $z = 5\,\mathrm{km}$ to visualise respectively the surface displacement and the pressure at depth.
- The strike–slip modulus for the strike–slip fault is $u_\theta = 1\,\mathrm{m}$, on the contrary for the normal and thrust faults it's zero. The dip–slip modulus for the normal fault is $u_\delta = 1\,\mathrm{m}$ and for the thrust fault is $u_\delta = -1\,\mathrm{m}$.
- The strike–slip fault has a dip angle $\delta = 90°$, the normal of $\delta = 60°$ and the thrust of $\delta = 30°$.

The elastic parameters have been chosen in order to replicate a medium solely composed of Berea sandstone. The following elastic parameters have been set in a configuration file:

- $\alpha = K/H = 1.0$ is the coefficient for the pore–pressure.
- $\rho = 2600\,\mathrm{kg\,m^{-3}}$ is the volumetric density of the rock.
- $B = 0.62$ is Skempton's coefficient.
- $D = 1.6\,\mathrm{m^2\,s^{-1}}$ is the mass diffusivity coefficient.
- $v_1 = 1.519\,\mathrm{km\,s^{-1}}$ is the velocity of the primary waves.
- $v_2 = 2.481\,\mathrm{km\,s^{-1}}$ is the velocity of the secondary waves.
- $\phi = 0.19$ is the porosity.

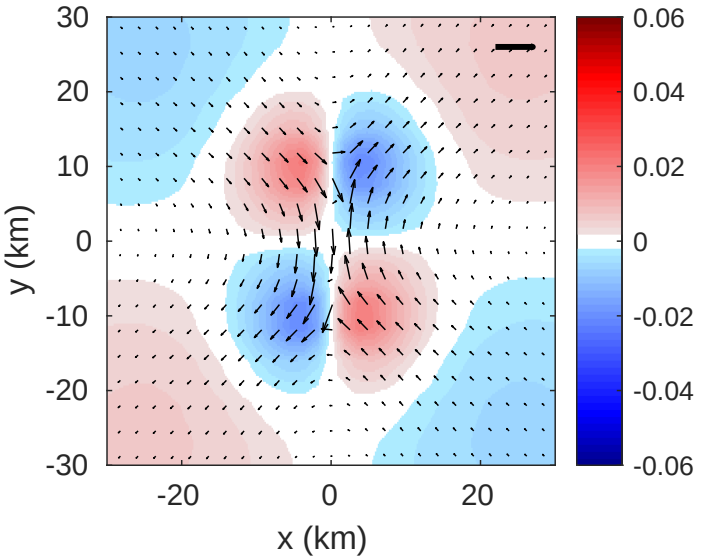

(a) Vertical displacement field u_3 (m) plot in a colour map at the initial instant $t = 0$ days at the surface depth of $z = 0$ km with the planar displacements vectors superimposed, for a strike–slip fault.

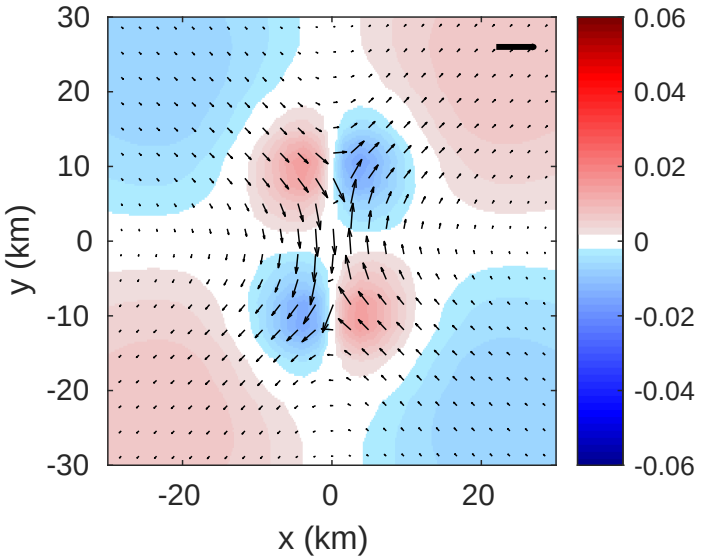

(b) Vertical displacement field u_3 (m) plot in a colour map at the instant $t = 51$ days at the surface depth of $z = 0$ km with the planar displacements vectors superimposed, for a strike–slip fault.

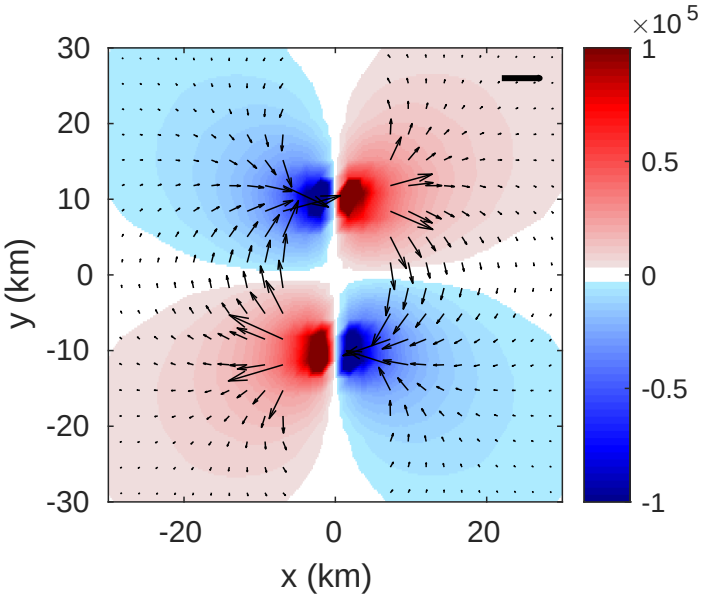

(c) Pore–pressure field p (Pa) plot in a colour map at the instant $t = 0$ days at the depth of $z = 5$ km with the planar Darcy's velocities vectors superimposed, for a strike–slip fault.

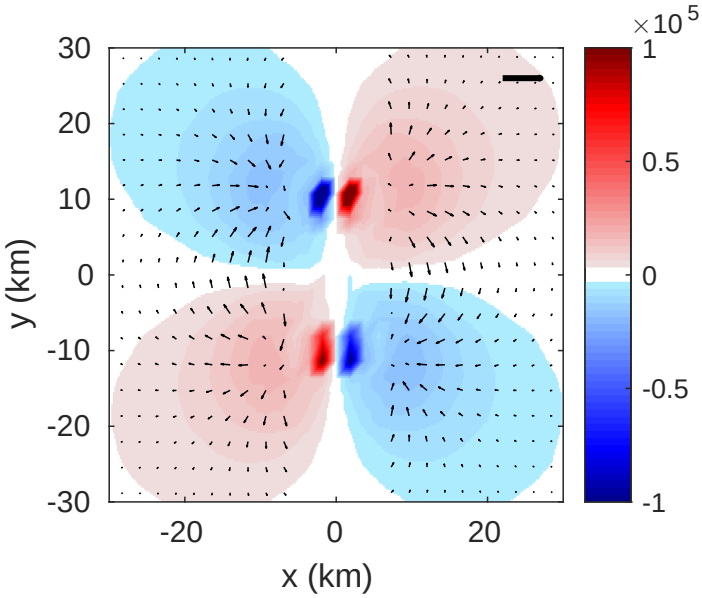

(d) Pore–pressure field p (Pa) plot in a colour map at the instant $t = 51$ days at the depth of $z = 5$ km with the planar Darcy's velocities vectors superimposed, for a strike–slip fault.

Figure 2.1: Strike–slip faulting events computed at different time instants and depths by the pegrn and pecmp software suite provided by Wang and Kümpel (2003). The vertical displacement is positive due to subsidence The bold arrow in the upper right corner of the figure is the scale: for the panels (a–b) it is 0.5 m, while for the panels (c–d) it is $10^{-9}\,\mathrm{m\,s^{-1}}$.

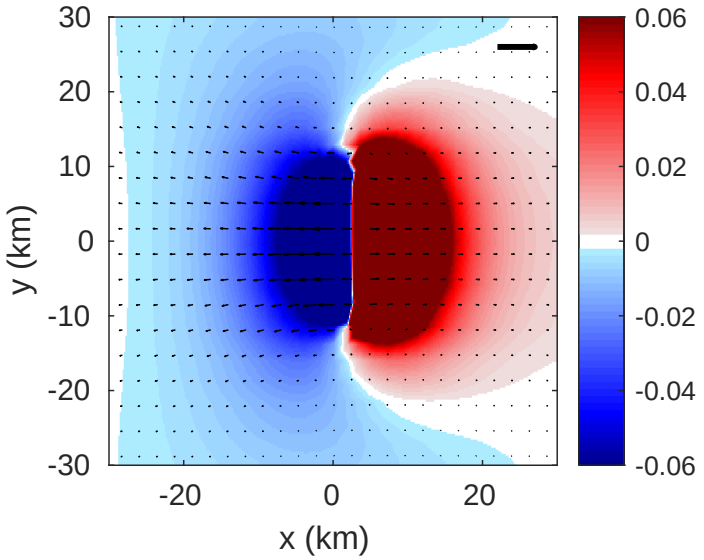

(a) Vertical displacement field u_3 (m) plot in a colour map at the initial instant $t = 0$ days at the surface depth of $z = 0$ km with the planar displacements vectors superimposed, for a normal fault.

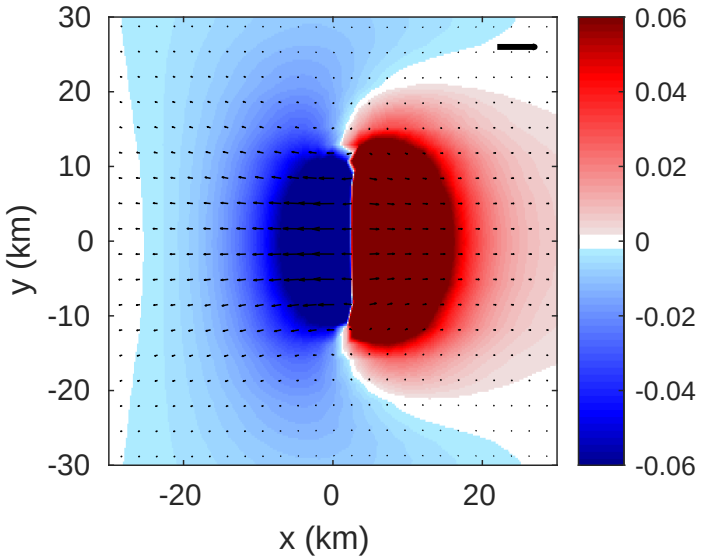

(b) Vertical displacement field u_3 (m) plot in a colour map at the instant $t = 51$ days at the surface depth of $z = 0$ km with the planar displacements vectors superimposed, for a normal fault.

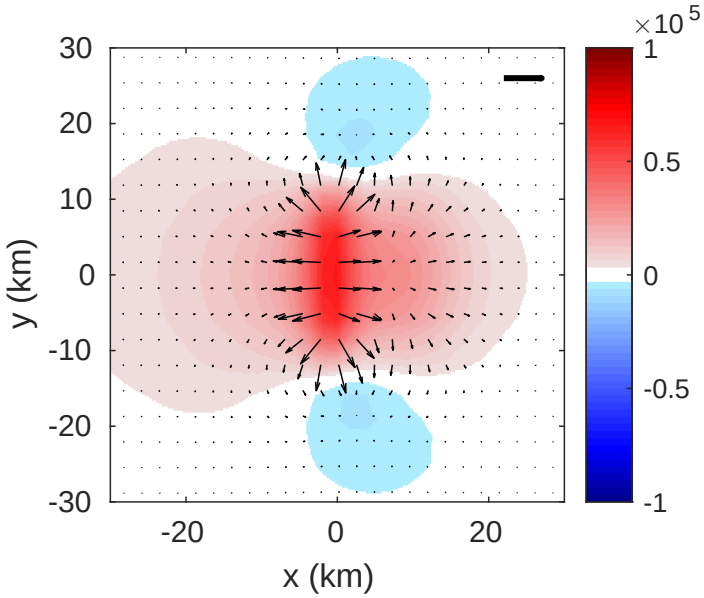

(c) Pore–pressure field p (Pa) plot in a colour map at the instant $t = 0$ days at the depth of $z = 5$ km with the planar Darcy's velocities vectors superimposed, for a normal fault.

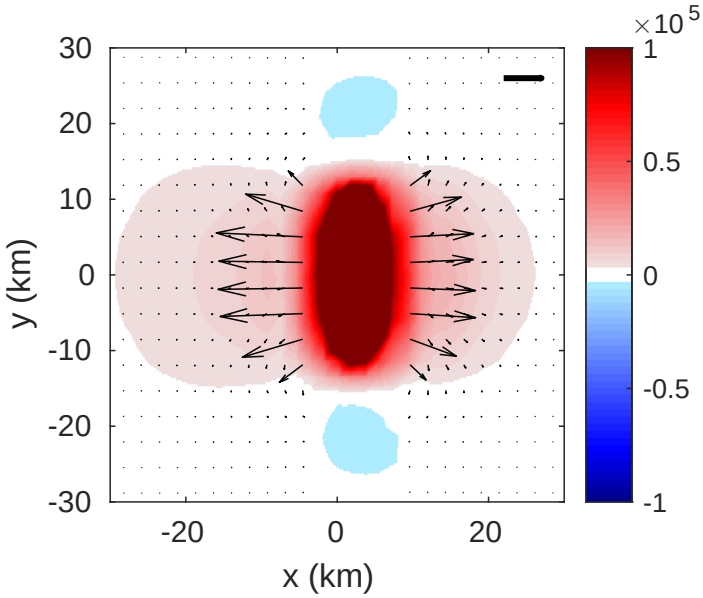

(d) Pore–pressure field p (Pa) plot in a colour map at the instant $t = 51$ days at the depth of $z = 5$ km with the planar Darcy's velocities vectors superimposed, for a normal fault.

Figure 2.2: Normal faulting events computed at different time instants and depths by the pegrn and pecmp software suite provided by Wang and Kümpel (2003). The vertical displacement is positive for subsidence. The vertical displacement is positive due to subsidence The bold arrow in the upper right corner of the figure is the scale: for the panels (a–b) it is 0.5 m, while for the panels (c–d) it is $10^{-9}\,\mathrm{m\,s^{-1}}$.

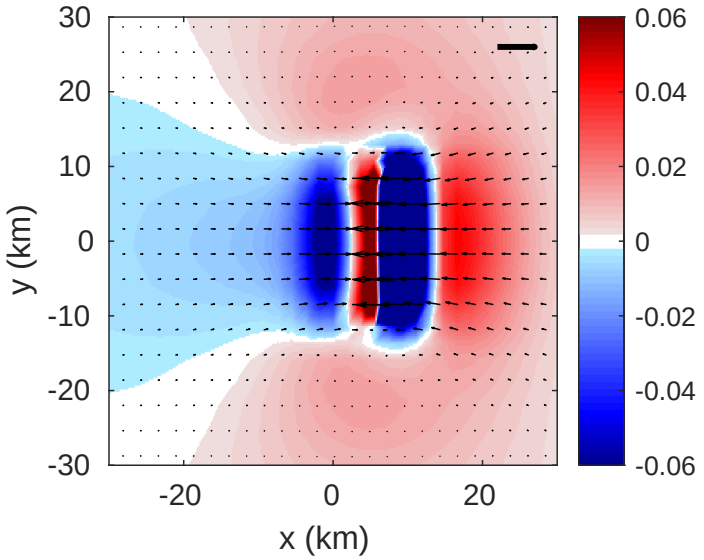

(a) Vertical displacement field u_3 (m) plot in a colour map at the initial instant $t = 0$ days at the surface depth of $z = 0$ km with the planar displacements vectors superimposed, for a thrust fault.

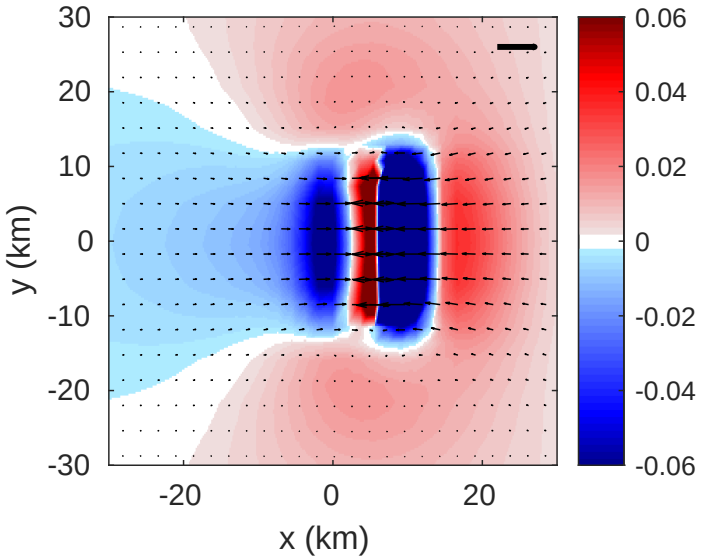

(b) Vertical displacement field u_3 (m) plot in a colour map at the instant $t = 51$ days at the surface depth of $z = 0$ km with the planar displacements vectors superimposed, for a thrust fault.

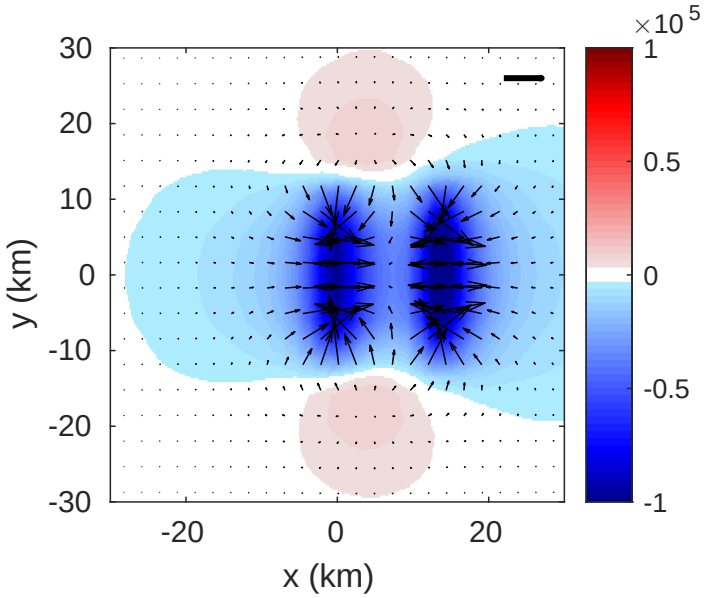

(c) Pore–pressure field p (Pa) plot in a colour map at the instant $t = 0$ days at the depth of $z = 5$ km with the planar Darcy's velocities vectors superimposed, for a thrust fault.

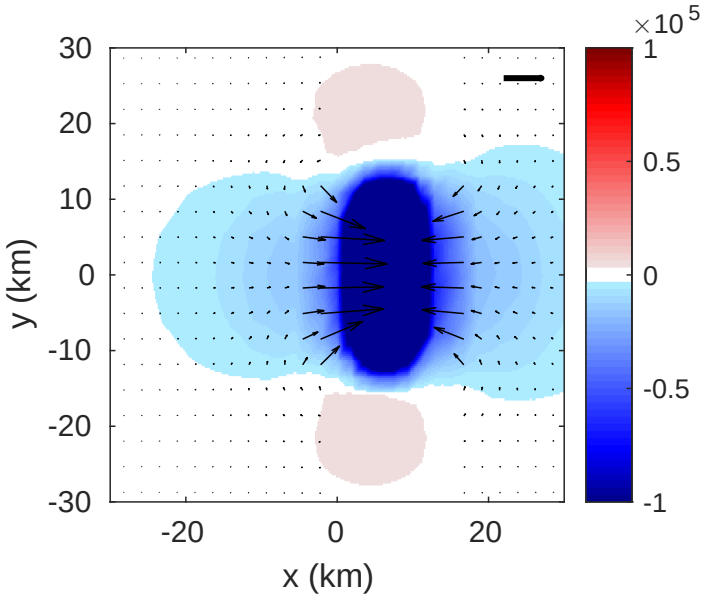

(d) Pore–pressure field p (Pa) plot in a colour map at the instant $t = 51$ days at the depth of $z = 5$ km with the planar Darcy's velocities vectors superimposed, for a thrust fault.

Figure 2.3: Thrust faulting events computed at different time instants and depths by the pegrn and pecmp software suite provided by Wang and Kümpel (2003). The vertical displacement is positive due to subsidence The bold arrow in the upper right corner of the figure is the scale: for the panels (a–b) it is 0.5 m, while for the panels (c–d) it is 10^{-9} m s^{-1}.

Chapter 3

Conclusions

In this chapter, results presented in the previous chapter regarding the strike–slip, normal and thrust fault types are analysed, expliciting the behaviour of the displacement and pore–pressure fields in the chosen time–frame.

Comparing the relative differences in magnitude of the vertical displacement at the surface, the rebound is most evident in the strike–slip fault for the considered time–frame of $\Delta t = 51$ days. The rebound is equally observed through the relative variations in pore–pressure at the depth of $z = 5$ km. They are equally evident in the normal and thrust faults, but less pronounced in the strike–slip.

3.1 Strike–slip fault

The strike-slip fault has a surface vertical displacement u_3, which has a double symmetry along the axes that reaches a maximum of 2 cm in modulus during the co–seismic phase. In each of the quadrants, the displacement varies pseudo–harmonically radially from the fault's center towards the outside. This produces a sort–of "butterfly" image pattern. The fact can also be expressed by noting that the associated pseudo–wavelength of the vertical displacement tends to shrinks as the time passes, limiting its extent.

The planar displacement field is aligned along the vertical direction, as the fault is hereby positioned and reaches a maximum value of 0.25 m in the co–seismic phase. The ground is displaced at the surface along both sides of the fault, immediately after the faulting process. This trend does not revert in time, Fig. (2.1b).

Fig. (2.1c–d) show that the pore–pressure p at a depth of $z = 5$ km appears to reduce in magnitude through time, without significant changes in the overall structure symmetry of the field.

In the domain of the field the pore–pressure reaches the maximum value of 1 bar near the fault, smoothening out as the distance from the fault increases.

Darcy's velocities suggest a flux of fluid exiting the positive pore–pressure zones (red) and entering the low pore–pressure ones (depicted in blue).

3.2 Normal fault

The positive displacement of the hanging wall is positive (subsidence), while in the foot wall is negative (uplift) in a coherent way to what is expected from a normal fault.

The pore–pressure at $z = 5\,\text{km}$ is almost fully positive and thus, this implies that the zone is subjected to co–seismic compression.

In the case of the normal fault, in Fig. (2.2a–b) the vertical displacement field u_3 at the surface is composed of lobes, positioned to the right and to the left of the fault, with the right lobe (in red) encompassing the fault. The vertical displacement u_3 reaches respectively a maximum value for $x > 0$ of about $0.41\,\text{m}$ and a minimum of about $-0.26\,\text{m}$ for $x < 0$, while the horizontal displacements reach a maximum modulus of about $18\,\text{cm}$.

Over time the left lobe which represents the depression of the ground reduces in size, as the right lobe representing the increase in height advances towards the left one while decreasing in width.

The pore–pressure field in Fig. (2.2c–d) at the depth of $z = 5\,\text{km}$ undergoes a very steep variation in time over the course of the chosen time–frame. Its maximum varies from about $0.64\,\text{bar}$ at $t = 0\,\text{days}$ to about $3.6\,\text{bar}$ at $t = 51\,\text{days}$ at it is registered at the centre of the domain. Darcy's planar velocities at this depth are out–flowing from the high pressure zone, which migrates to the centre of the fault over time, and at the same time increasing in magnitude, as seen in Fig. (2.2d).

The lateral low–pressure regions are of lesser importance, due to their magnitude being irrelevant to the scale of the phenomena.

3.3 Thrust fault

The vertical displacement reaches the minimum in the hanging wall for $x \approx 10\,\text{km}$, coherent with the one generated by a thrust fault.

The pore–pressure at z = 5 km is almost fully negative and thus, this implies that the zone is subjected to co–seismic dilation.

The comparison with the normal fault is highlighted in Fig. (2.3a–b) by the equal presence of lobes, one of high magnitude displacement and the other of lesser magnitude. The depression lobe (in blue) encompasses the fault, oriented vertically at the center of the plot. Over time, the surface displacement field shifts to the left, in the direction highlighted by the vector field.

The vertical displacements near the center of the domain reach a maximum of about $0.07\,\text{m}$ and a minimum of about $-0.33\,\text{m}$, while the horizontal ones have a maximum in modulus of $30\,\text{cm}$.

The pore–pressure at the depth of $z = 5\,\text{km}$ in Fig. (2.3c) is initially composed of low–pressure lobes, which reaches a minimum of about $-1\,\text{bar}$, which ends up merging in the observed time–frame, in order to form a very–low–pressure uniform zone located just to the right of the fault, as seen in Fig. (2.3d), which in itself reaches values of about $-5\,\text{bar}$. The later high–pressure regions are of lesser relevance, as their magnitude is

also in this case irrelevant to the study of the phenomena.

3.4 Closing statement

The objective of this thesis to simulate the poro–elastic rebound in the post–seismic phase of strike–slip, normal and thrust faults is deemed successful because the simulation data is seen to accurately reproduce the deformations observed in the near field in poro–elastic media due to strike–slip, normal and thrust faults. This is verifiable when comparing it to the data reported by Piombo et al. (2005) and Nespoli et al. (2016).

Bibliography

Belardinelli, M. E. and Bonafede, M. (2022). *Appunti dal Corso di Fondamenti di Geofisica 1*. Università di Bologna. `https://virtuale.unibo.it`.

Biot, M. A. (1941). General theory of three-dimensional consolidation. *Journal of Applied Physics*. 12 (2), pp.155-164. 10.1063/1.1712886 . hal-01368635.

Greenshields, C. and Weller, H. (2022). *Notes on Computational Fluid Dynamics: General Principles*. CFD Direct Ltd, Reading, UK.

Landau, L., Lifshits, E., Kosevich, A., Lifshitz, E., and Pitaevskii, L. (1986). *Theory of Elasticity: Volume 7*. Course of theoretical physics. Elsevier Science.

Nespoli, M., Todesco, M., Serpelloni, E., Belardinelli, M. E., Bonafede, M., Marcaccio, M., Rinaldi, A. P., Anderlini, L., and Gualandi, A. (2016). Modeling earthquake effects on groundwater levels: evidences from the 2012 emilia earthquake (italy). *Geofluids*, 16(3):452–463.

Palacios, R. (2023). deg2utm. *MATLAB Central File Exchange. Retrieved September 2, 2023*. `https://www.mathworks.com/matlabcentral/fileexchange/10915-deg2utm`.

Piombo, A., Martinelli, G., and Dragoni, M. (2005). Post-seismic fluid flow and Coulomb stress changes in a poroelastic medium. *Geophysical Journal International*, 162(2):507–515.

Ranalli, G. (1995). *Rheology of the Earth*. Springer Netherlands.

Rice, J. R. and Cleary, M. P. (1976). Some basic stress diffusion solutions for fluid-saturated elastic porous media with compressible constituents. *Reviews of Geophysics*, 14(2):227–241.

Scherbaum, F., Kuehn, N., and Zimmermann, B. (March 7 2011). Styles of faulting. *Wolfram Demonstrations Project*. `http://demonstrations.wolfram.com/StylesOfFaulting/`.

Wang, C.-Y. and Manga, M. (2021). Water and earthquakes. *Springer Cham*.

Wang, H. F. (2000). *Theory of Linear Poroelasticity with Applications to Geomechanics and Hydrogeology*. Princeton University Press.

Wang, R. and Kümpel, H.-J. (2003). Poroelasticity: Efficient modeling of strongly coupled, slow deformation processes in a multilayered half-space. *Geophysics*, 68(2):705–717.

Wolfram, S. (2022). https://writings.stephenwolfram.com/2022/06/launching-version-13-1-of-wolfram-language-mathematica/.

Wolfram, S. (2023). https://www.wolfram.com/mathematica/new-in-10/geo-related-properties/visualize-depth-and-position-of-earthquakes.html.